

# 1. Introduction

A generic channel model was presented for typical indoor and outdoor environments for evaluating 802.15.4a systems [21]. However, measurements of the radio channel around the human body indicate that some modifications are necessary to accurately model a body area network (BAN) scenario.

In order to characterize a BAN, we performed several Finite Difference Time Domain (FDTD) simulations of radio propagation around the human body. We then confirmed the resulting model by performing measurements and comparing with independent figures from the literature.

The conclusions of our BAN channel study are presented below. Section 2 describes the simulation environment and setup. Sections 3 – 5 summarize the simulated pathloss, power delay profile, and amplitude distributions. Section 6 focuses on the statistics of a deterministic cluster of multi-path components that was observed due to reflection off of the ground. Section 7 compares the simulated results with actual measurements taken around the body. Finally, section 8 describes a Matlab implementation of the complete channel model.

## 2 Simulation Setup

The Remcom Finite Difference Time Domain (FDTD) Simulator [1] was used to model electromagnetic field propagation around the human body. An anatomically correct model of a body was provided by the Visual Human project of the National Library of Medicine [2]. This body mesh is accurate to within 5 cubic mm allowing frequencies up to 6 GHz to be simulated correctly [3].

Channel characteristics were extracted in the time domain by transmitting a wideband Gaussian pulse and recording the magnitude of the z-component of the electromagnetic field around the human torso. The transmitted pulse had a 10 dB bandwidth of approximately 4 GHz spanning the range between 2 and 6 GHz. Real antennas were not used in the simulator. Rather, an electric field was generated directly by applying a voltage across one of the FDTD cells, and then observing how the electromagnetic wave propagates.

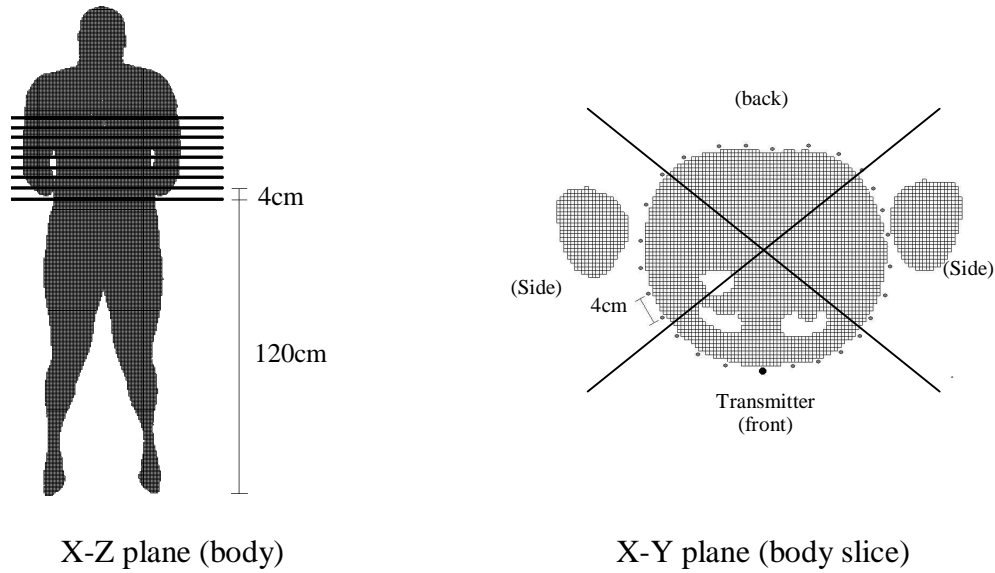


**Figure 1 Simulation Setup**

Figure 1 shows the simulation setup. All channel parameters were extracted from nine simulations performed in planes separated by 4 cm along the z-axis of the torso (see left diagram). For each of these nine simulations, the transmitter was placed on the front of the torso. Measurements were taken in the x-y plane at several positions separated by 4 cm around the human torso (see right diagram). In all cases, both the transmitter and receiver were placed 5 mm away from the body. To increase the number of points for extracting channel statistics, measurements one plane above and one plane below the transmitter were recorded in each simulation. In this way, a total of 570 measurements were taken at various positions around the body.

We found that the channel parameters changed depending on the position of the body. To describe this phenomenon easily, we defined three regions representing the front, side, and back of the body (see right diagram). The front region corresponds to measurements taken between  $0$  to  $\pm 60^\circ$ , the side region corresponds to measurements taken between  $\pm 60^\circ$  to  $\pm 120^\circ$ , and the back region corresponds to measurements taken between  $\pm 120^\circ$  and  $\pm 180^\circ$ .

### 3 Path loss

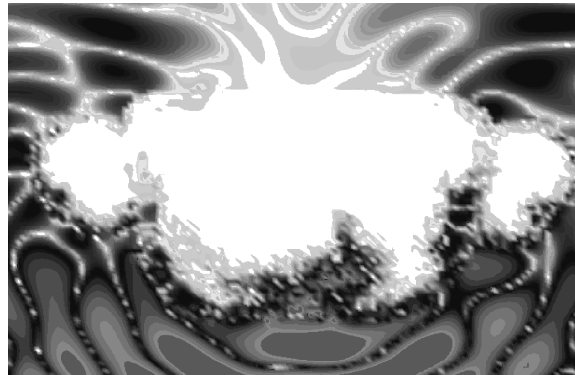


**Figure 2 Electric Field Magnitude around Body**

Figure 2 shows an electric field snapshot in the x-y plane taken 5 ns after transmitting a pulse. The different shades of gray correspond to different field magnitudes: black represents a large magnitude, while lighter colors represent a smaller magnitude. The white area in the center of the diagram is due to the arms and torso. This indicates that very little energy is inside of the body in the GHz range. Instead, the wave is diffracting *around* the torso rather than passing through it. Therefore in calculating the path loss, we measure the distance around the perimeter of the body. This is in contrast to previous measurement campaigns in the GHz frequencies where the path loss model was erroneously assumed to be related to the straight-line distance through the body [4, 5].

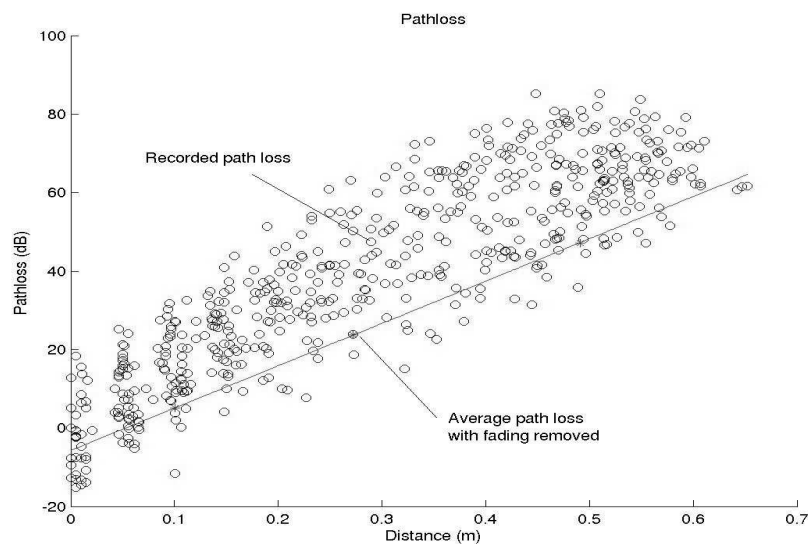


**Figure 3 Pathloss**

Figure 3 shows the path loss versus distance trend. The vertical axis represents the attenuation of the signal power relative to the signal power recorded at a reference distance 4 cm away from the transmitter. The horizontal axis is the distance traveled by the wave around the perimeter of the body. The circles indicate individual measurements. It is clear that the path loss decreases with distance as expected, and that there is a large fading variance. In order to extract a path loss model, the fading was removed by averaging the measurements on the front, side, and back of the body in the linear domain. The resulting points are represented by asterisks together with a best-fit line. The fading distribution around the mean will be discussed in section 5.

Contrary to previous measurements [4, 5], the more extensive data set presented here shows that the path loss near the body increases exponentially with distance:

$$P_{dB} = \gamma(d - d_0) + P_{0dB} \quad (1)$$

$\gamma$  is in units of dB/meter,  $d$  is the distance from the antenna,  $d_0$  is the reference distance, and  $P_0$  is the power at the reference distance. The parameters of this path loss model extracted from the simulator are shown in table 1. Note that the simulator does not provide a realistic reference power since the electric field is generated by applying a voltage across an FDTD cell rather than using a real antenna. Therefore, the reference power in table 1 was obtained with a real measurement setup. This will be discussed further in section 5.6.

Parameter	Value
$\gamma$	107.8 dB/m
$d_0$	0.1 m
$P_0$	35.5 dB

**Table 1 Pathloss model**

Because of the large bandwidth of an UWB pulse, a frequency-dependent path loss has been proposed in [6,7]. In order to determine whether this model is required for body area networks operating in the GHz frequencies, we repeated the above simulation but transmitted sinusoids at 2,3,4,5, and 6 GHz. We measured a slight increase in the path loss with increasing frequency. However, there was only a negligible 6% difference in  $\gamma$  between the 2 and 6 GHz. We will therefore assume a frequency independent path loss.

## 4 Power Delay Profile

A convenient characterization of multi-path propagation channels is the discrete-time impulse response model [8,9,10,11]. In this model, the time axis is divided into small time intervals called “bins”. The received power is integrated within each bin to obtain the energy received as a function of the excess delay. The first bin corresponds to the first received MPC and its location is determined manually. If the energy in subsequent bins is 20 dB less than the energy in the strongest bin, then we assume this bin does not contain any significant multi-path components and it is assigned a value of zero. Otherwise, the bin is assumed to contain a single MPC with an amplitude

corresponding to the energy measured in that bin. The bin size is generally chosen to be the resolution of the specific measurement, since two paths arriving within a bin cannot be resolved. In our case, we selected a bin width of 0.5 ns.

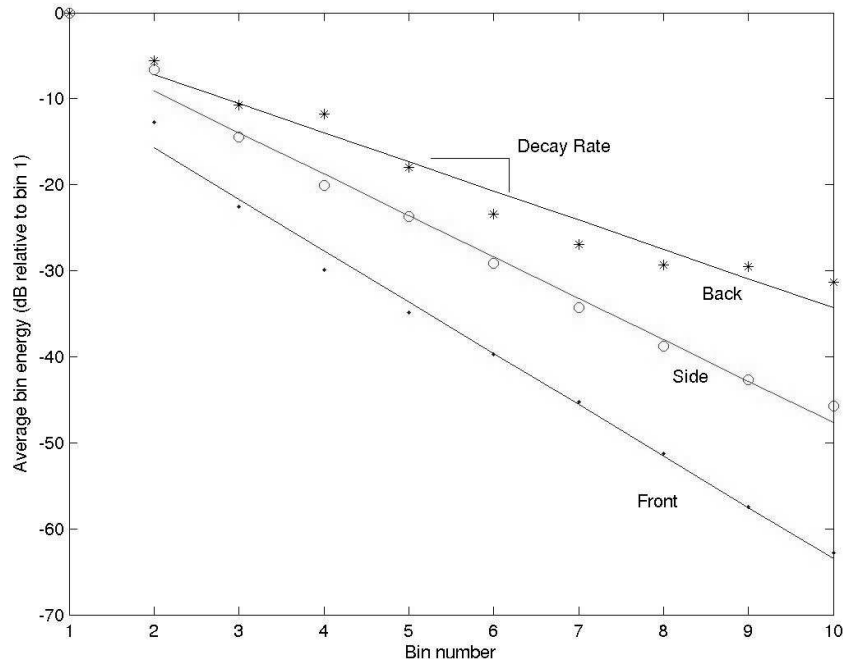


**Figure 4 Average Power Delay Profile**

By averaging the power in each bin over all the measurements, we can obtain the average power delay profile (see Figure 4). The vertical axis shows the average bin power relative to the average power in the first bin. The horizontal axis indicates the bin number where the width of one bin is 0.5 ns. Individual points indicate the average power in each bin, while the straight line is obtained by a best-fit procedure. Clearly, the energy of subsequent MPCs decays exponentially with delay in a similar manner as in typical multi-path environments [12]. This is illustrated by the excellent linear fit on a decibel scale. The decay rates depend on the position of the body and are summarized in Table 5 together with the average energy of the second MPC relative to the first bin. Both simulated and measured results are provided in the same table.

In general, there is a longer impulse response on the back of the body compared with the front of the body. This is in agreement with past measurements taken around the human torso [5]. Since only negligible energy was observed inside the body, this effect is probably due to echoes off of the body itself. For example, the signal can diffract around the body in both counter clockwise and clockwise directions, as well as around the shoulders and arms.

## 5. Amplitude Distribution

In addition to the large-scale path loss trend around the human body, a reliable statistical model is needed to determine how much the signal level can vary. To our knowledge, the amplitude distribution around the human body has never been studied.

In UWB systems, each resolved MPC is due to a small number of scatterers and the amplitude distribution in *each* bin can be different [10]. Therefore we extract the amplitude distribution of every bin individually.

To determine the amplitude distribution, the large-scale path loss (the straight line from Figure 3) was removed so that the average path loss on the front, side and back of the body was unity. Several distributions were fit to the resulting data including Nakagami-m, Rayleigh, Lognormal, and Suzuki distributions. We used the parameter estimators from [13] for the Nakagami-m distribution. We used the estimators from [14] for all other distributions. It was clear that only the lognormal and Suzuki models provided a reasonable fit. The other distributions could be rejected based on visual inspection of the empirical and fit distributions, and because they consistently failed both the  $\chi^2$  and Kolmogorov goodness-of-fit tests [15] with a significance level of less than 1% for each bin<sup>1</sup>. The resulting Suzuki and lognormal distributions were very similar. Therefore, we recommend using a lognormal distribution as it is much easier to implement.

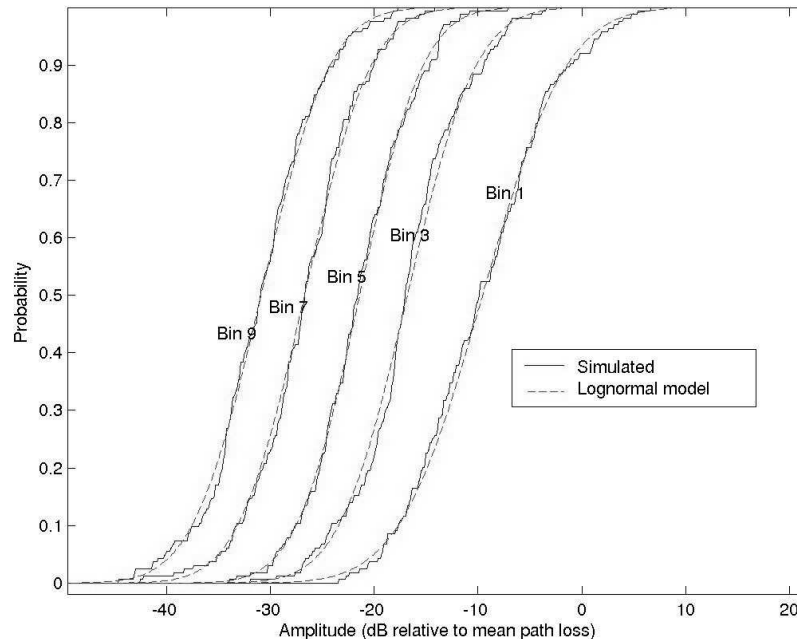


**Figure 5 Amplitude Cumulative Density Functions (side of body)**

---

<sup>1</sup> We also applied the Akaike Criterion for comparing models. The Suzuki and Lognormal distributions were approximately equally likely the best model. The other distributions had only a negligible probability of being the best model.

Empirical and theoretical lognormal-fit distributions obtained along the side of the body for several bins are reproduced in Figure 5. Visual inspection of these figures show an excellent lognormal fit to the data.

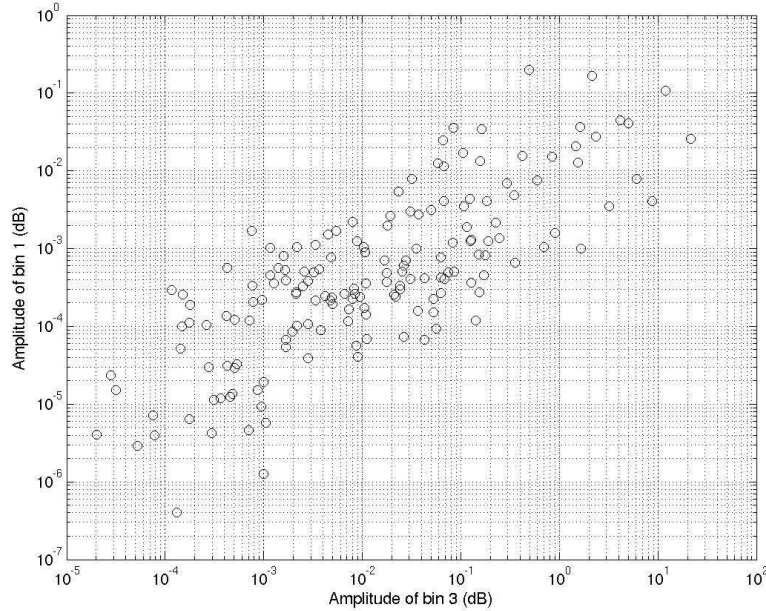


**Figure 6 Correlation between bins 1 and 3 (side of body)**

Figure 6 shows a plot of the bin 1 amplitudes versus bin 3 amplitudes recorded along the side of the body. This plot clearly demonstrates a significant correlation between bins. While correlated MPCs is not typical of traditional indoor wireless channels [16], high correlation coefficient at the small excess delays encountered here have been reported in the past [17,18]. This correlation could be due to any of the following three effects:

1. Spreading of the pulse due to a frequency-selective pathloss.
2. Multipath components regularly arriving at the boundary of two adjacent bins.
3. The uncorrelated scattering assumption [16] was violated.

The first effect is not likely important since we did not measure a frequency-selective path loss in section 5.2. The second effect may have contributed to the correlation we observed. However, we also found significant correlation between non-adjacent bins (Figure 6) indicating that the third reason is probably the most important factor. Physical phenomenon that may have contributed to correlated multi-path components include an overlap in path trajectories propagating close to the body especially in the vicinity of the transmitter and receiver, very short path lengths, and a natural symmetry of the body.

Table 2 summarizes the simulated mean, the variance, and the correlation matrices of the log amplitudes. The mean and variance are in dB units and relative to the mean path loss computed in section 5.2. The correlation coefficient between bin  $j$  and bin  $k$  is defined as follows:

$$\rho_{j,k} = \frac{E[(G_j - \overline{G_j})(G_k - \overline{G_k})]}{\sqrt{E[(G_j - \overline{G_j})^2]E[(G_k - \overline{G_k})^2]}}$$

Where  $G_k$  represents the log amplitude at bin number  $k$ . Note that this is the log-correlation coefficient rather than the more traditional linear correlation coefficient. We have chosen to use the log-correlation since it is more convenient for generating correlated lognormal variables in a channel simulator (see section 8). The correlation matrix,  $R$ , shows the log correlation between the bin in row  $j$  and the bin in column  $k$ .

$$R_{\text{side}} = \begin{bmatrix} 1 & 0.9 & 0.78 & 0.77 & 0.73 & 0.64 & 0.62 & 0.53 & 0.53 & 0.45 \\ 0.9 & 1 & 0.88 & 0.83 & 0.77 & 0.74 & 0.72 & 0.64 & 0.64 & 0.59 \\ 0.78 & 0.88 & 1 & 0.84 & 0.76 & 0.77 & 0.76 & 0.7 & 0.69 & 0.66 \\ 0.77 & 0.83 & 0.84 & 1 & 0.86 & 0.81 & 0.81 & 0.74 & 0.75 & 0.73 \\ 0.73 & 0.77 & 0.76 & 0.86 & 1 & 0.85 & 0.83 & 0.74 & 0.72 & 0.69 \\ 0.64 & 0.74 & 0.77 & 0.81 & 0.85 & 1 & 0.92 & 0.81 & 0.75 & 0.72 \\ 0.62 & 0.72 & 0.76 & 0.81 & 0.83 & 0.92 & 1 & 0.86 & 0.81 & 0.77 \\ 0.53 & 0.64 & 0.70 & 0.74 & 0.74 & 0.81 & 0.86 & 1 & 0.92 & 0.86 \\ 0.53 & 0.64 & 0.69 & 0.75 & 0.72 & 0.75 & 0.81 & 0.92 & 1 & 0.91 \\ 0.45 & 0.59 & 0.66 & 0.73 & 0.69 & 0.72 & 0.77 & 0.86 & 0.91 & 1 \end{bmatrix}$$

$$R_{\text{front}} = \begin{bmatrix} 1 & 0.86 & 0.56 & 0.66 & 0.66 & 0.51 \\ 0.86 & 1 & 0.74 & 0.74 & 0.73 & 0.59 \\ 0.56 & 0.74 & 1 & 0.82 & 0.79 & 0.71 \\ 0.66 & 0.74 & 0.82 & 1 & 0.87 & 0.62 \\ 0.66 & 0.73 & 0.79 & 0.87 & 1 & 0.76 \\ 0.51 & 0.59 & 0.71 & 0.62 & 0.76 & 1 \end{bmatrix}$$

$$R_{\text{back}} = \begin{bmatrix} 1 & 0.88 & 0.84 & 0.78 & 0.55 & 0.59 & 0.54 & 0.48 & 0.62 & 0.72 \\ 0.88 & 1 & 0.91 & 0.76 & 0.70 & 0.74 & 0.63 & 0.57 & 0.71 & 0.81 \\ 0.84 & 0.91 & 1 & 0.81 & 0.68 & 0.80 & 0.72 & 0.63 & 0.74 & 0.81 \\ 0.78 & 0.76 & 0.81 & 1 & 0.69 & 0.69 & 0.79 & 0.68 & 0.69 & 0.70 \\ 0.55 & 0.70 & 0.68 & 0.69 & 1 & 0.83 & 0.76 & 0.84 & 0.82 & 0.82 \\ 0.59 & 0.74 & 0.80 & 0.69 & 0.83 & 1 & 0.85 & 0.84 & 0.83 & 0.81 \\ 0.54 & 0.63 & 0.72 & 0.79 & 0.76 & 0.85 & 1 & 0.86 & 0.77 & 0.71 \\ 0.48 & 0.57 & 0.63 & 0.68 & 0.84 & 0.84 & 0.86 & 1 & 0.85 & 0.77 \\ 0.62 & 0.71 & 0.74 & 0.69 & 0.82 & 0.83 & 0.77 & 0.85 & 1 & 0.91 \\ 0.72 & 0.81 & 0.81 & 0.70 & 0.82 & 0.81 & 0.71 & 0.77 & 0.91 & 1 \end{bmatrix}$$

Bin	Front		Side		Back	
	$\mu_{dB}$	$\sigma_{dB}$	$\mu_{dB}$	$\sigma_{dB}$	$\mu_{dB}$	$\sigma_{dB}$
1	5.7	4.7	9.6	6.3	9.2	6.3
2	12.1	4.2	12.9	5.7	12.0	6.5
3	17.0	5.2	16.8	5.2	14.6	6.3
4	20.7	5.1	19.6	5.0	15.1	5.7
5	23.2	5.1	21.4	4.8	18.2	5.4
6	25.6	4.5	24.1	4.8	20.9	5.7
7	28.4	4.6	26.7	5.0	22.7	5.5
8	31.4	4.6	28.9	5.0	23.9	5.2
9	34.5	4.8	30.9	5.2	24.0	5.1
10	37.1	4.7	32.4	5.6	24.9	5.4

Table 2 Amplitude Distributions for Each Bin

## 6. Ground Reflections

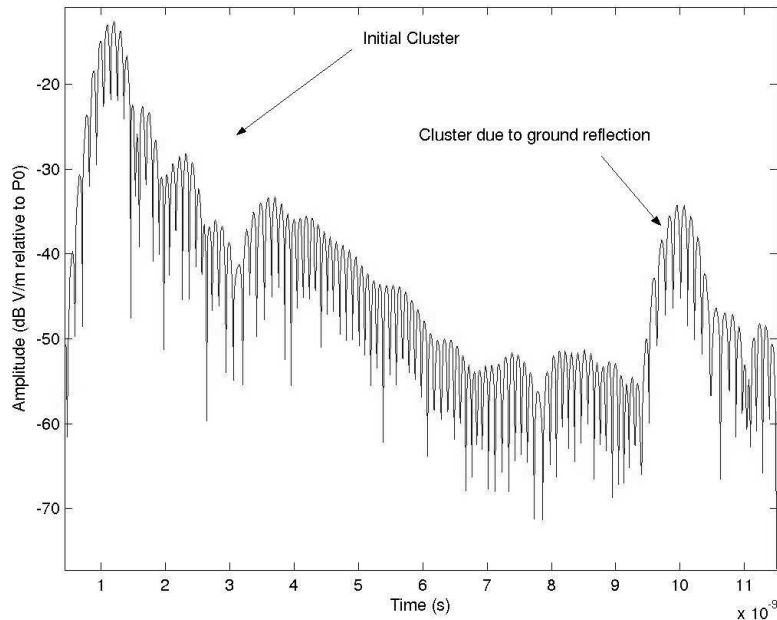


**Figure 7 Ground Reflection (front of body)**

Figure 7 shows the impulse response plotted on a logarithmic scale recorded at a position on the front of the body. There are two clear clusters of multi-path components. The first cluster is due to diffraction of the wave around the torso. This cluster of components was explored in the previous two sections. The second cluster is due to a reflection off of the ground and was also observed in [5]. We were able to confirm that this cluster was due to a ground reflection in two ways. First, its arrival time was consistent with the distance traveled by the pulse. Second, when we replaced the floor in the simulator by a perfectly absorbing material, the cluster was no longer observed. While the second cluster is much smaller than the first cluster on the front of the body, it becomes important on the back and side of the body where the initial wave is significantly attenuated.

Reflections off the ground were analyzed by including a floor made of a perfect electrical conductor (PEC) in the simulation geometry, and then binning the second cluster of components in the same manner as in sections 4 and 5. As in the initial cluster, the MPCs reflecting off the ground were well modeled by correlated lognormal variables. The resulting amplitude distributions for the first three bins are summarized in Table 3 together with the correlation matrices. The mean path loss is given relative to the reference path loss near the antenna,  $P_0 = 35.5$  dB, from Table 1.

$$\mathbf{R}_{\text{floorf}} = \begin{bmatrix} 1 & 0.91 & 0.76 \\ 0.91 & 1 & 0.84 \\ 0.76 & 0.84 & 1 \end{bmatrix} \quad \mathbf{R}_{\text{floors}} = \begin{bmatrix} 1 & 0.93 & 0.79 \\ 0.93 & 1 & 0.85 \\ 0.79 & 0.85 & 1 \end{bmatrix} \quad \mathbf{R}_{\text{floorb}} = \begin{bmatrix} 1 & 0.96 & 0.89 \\ 0.96 & 1 & 0.9 \\ 0.89 & 0.9 & 1 \end{bmatrix}$$

	Front		Side		Back	
Bin	$\mu_{\text{dB}}$	$\sigma_{\text{dB}}$	$\mu_{\text{dB}}$	$\sigma_{\text{dB}}$	$\mu_{\text{dB}}$	$\sigma_{\text{dB}}$
1	24.4	4.3	28.8	5.2	29.3	4.9
2	28.7	4.4	32.2	5.0	33.0	4.7
3	29.3	4.3	37.4	5.4	40.0	5.5

**Table 3 Amplitude Distributions for Ground Reflection off a perfect electrical conductor (PEC)**

Note that there was also some correlation detected between bins due to ground reflections and bins in the first cluster, particularly along the front of the body ( $\rho \approx 0.6$ ). However, along the side and back of the body, where the ground reflection component becomes significant, these bins were only weakly correlated ( $\rho$  between 0.3 and 0.4). We will therefore assume the first and second clusters are statistically independent in our model.

The values in table 4 vary depending on the electrical properties of the floor materials. To quantify the impact of different kinds of floors, additional simulations were conducted for concrete, and average outdoor ground conditions. In general, the same distributions were observed, but an additional path loss needed be incorporated to take into account the extra loss due to the reflection (see Table 4).

Material	Conductance (S)	Relative Permittivity	Loss relative to PEC (dB)
Concrete	0.01	5	6.0
Average Ground	0.005	15	1.1

**Table 4 Additional path loss for different ground materials**

## 7. Measurement Results

The results of the previous sections were compared with measurements taken around the body. These measurements were performed outdoors in a parking lot so that only the initial diffracted waves and the ground reflections were observed. The measurements were taken in the 3 to 5 GHz band. A network analyzer and two meander line antennas (Skycross SMT-3TO6M) [19] were used to determine the S-Parameter  $S_{21}$ .

The same setup was used as in Figure 1. However, only two distances around the body were analyzed: 10 cm and 20 cm from the transmitter. The first distance was located along the front of the body, while the second distance was located along the side of the body. At each distance, 8 measurements were made at positions along the height of the torso separated by approximately 5 cm. In all cases, the antennas were adhered to the body using tape.

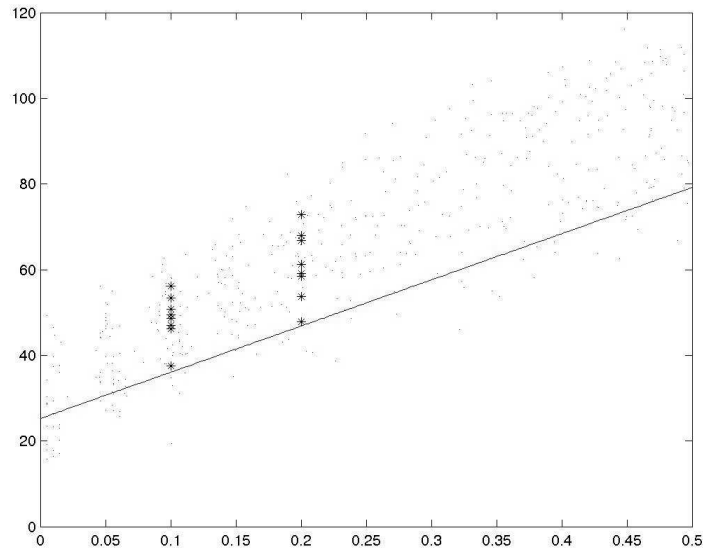


**Figure 8 Simulated and measured Pathloss**

Figure 8 compares the simulated path loss model with the measured path loss. The small dots represent simulation results, while the asterisks represent actual measurements. The solid line is the path loss model derived from table 2. Clearly, there is a close match between the simulated and measured path loss trends. This setup was also used to estimate a realistic reference path loss,  $P_0$ , from table 2 based on the mean path loss at a distance of  $d_0 = 10$  cm.

<b>Position</b>	<b>Simulated decay rate (dB/ns)</b>	<b>Measured decay rate (dB/ns)</b>	<b>Simulated Bin 1 and 2 power ratio (dB)</b>	<b>Measured Bin 1 and 2 power ratio (dB)</b>
Front	-11.9	-9.0	-15.7	-9.3
Side	-9.6	-8.8	-9.1	-8.6
Back	-6.8	N/A	-7.2	N/A

**Table 5 Average Power Delay Profile**

The simulated and measured average power delay profiles are compared in table 6. While the results match closely along the side of the body, a somewhat longer impulse response was measured along the front of the body. This may be due to a smaller sample size, antenna coupling and filtering effects not accounted for in the simulation environment, or the larger physical size of the simulated body. As in the simulated results, a large log-correlation coefficient ranging between 0.75 – 0.90 was observed between bins extracted from the measured data.

Based on this study, we conclude that the simulator is functioning properly since it yields statistics similar to those measured around the body. In the future, more measurements will be made to better characterize any differences between the simulated and measured channels.

## 8 Model Implementation

Implementing this model on a computer involves generating  $N$  correlated lognormal variables representing the different bins, and then applying an appropriate path loss based on the distance between the antennas around the body. This can be accomplished by generating  $N$  correlated normal variables, adding the pathloss, and then converting from a dB to linear scale. Thus, the only information needed to simulate the channel is contained in tables 1-3.

To generate correlated normal variables, we follow the procedure given in [20]. First we generate the covariance matrix  $C$  using the appropriate correlation coefficients and standard deviations in tables 2-3 corresponding to the desired scenario (front, side, or back of body):

$$C = \begin{bmatrix} \sigma_1^2 & \rho_{1,2}\sigma_1\sigma_2 & \cdots & \rho_{1,N}\sigma_1\sigma_N \\ \rho_{2,1}\sigma_2\sigma_1 & \sigma_2^2 & \cdots & \rho_{2,N}\sigma_2\sigma_N \\ \cdots & \cdots & \cdots & \cdots \\ \rho_{N,1}\sigma_N\sigma_1 & \cdots & \cdots & \sigma_N^2 \end{bmatrix} \quad (2)$$

We then generate a vector  $X$  of  $N$  uncorrelated, unit mean, unit variance normal variables where  $N$  is the number of filter taps in the channel.  $X$  is post multiplied by the upper triangular Cholesky factorization of  $C$  to introduce the correlation [20], the mean amplitude of each bin ( $M$ ) is added, and the appropriate pathloss ( $P_{dB}$ ) is applied. This procedure can be summarized by the following equation:

$$Y = X \cdot chol(C) + M - \frac{P_{dB}}{2} \quad (3)$$

$M$  is a vector of  $N$  means obtained from tables 2-3 for the appropriate scenario, and  $P_{dB}$  is the path loss obtained from equation (1) and table 1. The resulting channel realization  $Y$ , a vector of  $N$  correlated normal variables, is then converted from the dB domain to the linear domain.

This process of generating correlated lognormal variables can be done for both the initial cluster and the ground reflection cluster. The arrival time between these clusters can be estimated based on the distance between the antennas and their height off the ground. For the body in our simulator, the arrival time ranged between 6 - 9.9 ns along the front, 6.5 - 9.5 ns along the side, and 5.5 - 8.5 ns along the back. To simplify this, we used a single mean value for each position (8.7 ns, 8 ns, and 7.4 ns).

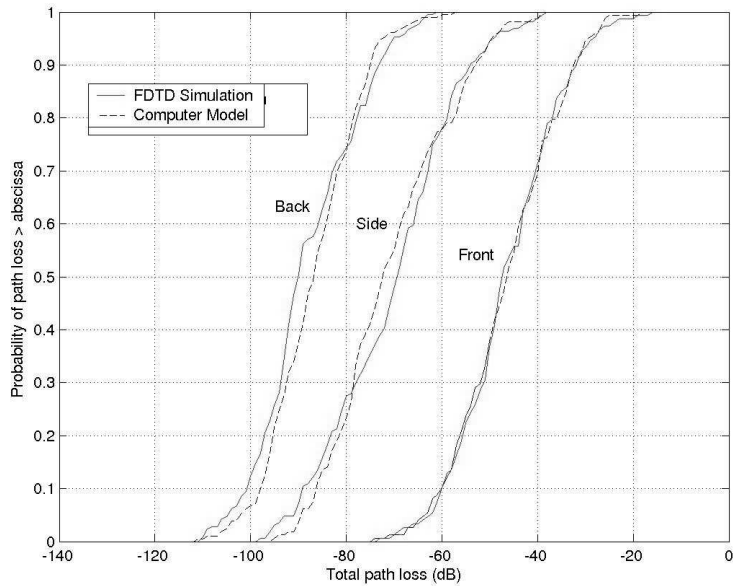


**Figure 9 Comparison of simulation and model signal quality**

	FDTD Simulated delay spread (ns)	Computer model delay spread (ns)
Front	0.3	0.4
Side	1.2	1.4
Back	2.0	1.9

**Table 6 Comparison of simulation and model delay spreads**

To test the model implementation, we used the same approach presented in [10] where the signal quality of the simulated data is compared with the data generated from our model. The signal quality is defined as the total averaged energy received at a given transmit-receiver separation relative to the transmitted power. Clearly, our model provides a very good match to the data. Another convenient metric commonly used to describe the channel impulse response is the rms delay spread [16]. Table 6 shows that channels generated with our model have similar delay spreads as the simulated channels. Small differences can likely be attributed to some of the simplifications we made including the first and second clusters being completely uncorrelated, and having a fixed arrival time.

## References

- [1] Remcom. [Online]. Available: <http://www.remcom.com>
- [2] Visible Human Project. [Online]. Available: [http://www.nlm.nih.gov/research/visible/visible\\_human.html](http://www.nlm.nih.gov/research/visible/visible_human.html)
- [3] K. S. Kunz and R. J Luebbers, *The Finite Difference Time Domain Method for Electromagnetics*, CRC Press.
- [4] Ghent University study (submitted)
- [5] T. Zasowski, F. Althaus, M. Stager, A. Wittneben, G. Troster, "UWB for noninvasive wireless body area networks: channel measurements and results," *2003 IEEE Conference on Ultra Wideband Systems and Technologies*, 16-19 Nov. 2003 Pages: 285 – 289.
- [6] J. Kunisch and J. Pamp, "Measurement results and modeling aspects for the UWB radio channel," in *IEEE Trans. On Vehicular Technology*, vol. VT-48, pp. 1204-1316, July 1999.
- [7] A. Alvarez, G. Valera, M Lobeira, R. Torres, and J. Garcia, "New channel impulse response model for UWB indoor system simulations," *Proc. VTC 2003*, p. 1-5 2003.
- [8] R. Ganesh and K. Pahlavan, "Statistical modeling and computer simulation of the indoor radio channel," *IEE Proc. Part I: Communication, Speech and Vision*, vol. 138, no. 3, pp. 153-161, June 1991.
- [9] H. Hashemi, "Impulse response modeling of indoor radio propagation channels," *IEEE J. Selected Areas Comm.*, vol 11, no 7, pp. 967-977, Sep. 1993.
- [10] D. Cassioli, M. Z. Win and A. F. Molisch, "The ultra-wide bandwidth indoor channel: from statistical model to simulations," *IEEE J. Selected Areas Comm.*, vol. 20, no. 6, pp. 1247-1257, Aug. 2002.
- [11] H. Hashemi, "The Indoor Radio Propagation Channel", *Proceedings of the IEEE*, vol. 81, no. 7, July 1993.
- [12] A. Saleh and R. A. Valenzuela, "A statistical model for indoor multipath propagation," *IEEE J. Selected Areas Comm.*, vol. 5, Feb. 1987.
- [13] Q. T. Zhang, "A note on the estimation of Nakagami- $m$  Fading Parameter", *IEEE Communication Letters*, vol. 6, No. 6, June 2002.
- [14] Alan J Coulson. "Characterization of the Mobile Radio Multipath Fading Channel." [Online]. Available: <http://www.irl.cri.nz/ofdm/images/publications/thesis.pdf>
- [15] R. Bartoszynski and M. Niewiadomska-Bugaj, *Probability and Statistical Inference*. New York, NY, USA: Wiley, 1996.
- [16] B. Sklar, "Rayleigh fading channels in mobile digital communication systems part I: Characterization," *IEEE Communicatinos Magazine*, vol. 35, no. 7, pp. 90-100, 1997.
- [17] G. L. Turin, F.D Clapp, T. L. Johnston, S. B. Fine, and D. Lavry, "A statistical model of urban multipath propagation," *IEEE Trans. Veh. Technology*, vol. VT-21, pp. 1-9, Feb. 1972.
- [18] T. S. Rappaport, S. Y. Seidel, and K. Takamizawa, "Statistical channel impulse response models for factory and open plan building radio communication system design," *IEEE Trans. Comm.*, vol. 39, no. 5, pp. 794-807, May 1991.
- [19] Skycross. [Online]. Available: <http://www.skycross.com>
- [20] Petyon Z. Peebles, Jr. *Probability, Random Variables, and Random Signal Principles*. New Jersey: McGraw-Hill, 1993.
- [21] Final Channel Model Report for 802.15.4a.